ARTICLES

Lattice strains in gold and rhenium under nonhydrostatic compression to 37 GPa

Thomas S. Duffy

Department of Geosciences, Princeton University, Princeton, New Jersey 08544

Guoyin Shen

Consortium for Advanced Radiation Sources, The University of Chicago, Chicago, Illinois 60637

Dion L. Heinz

Department of Geophysical Sciences, The University of Chicago, Chicago, Illinois 60637

Jinfu Shu, Yanzhang Ma, Ho-Kwang Mao, and Russell J. Hemley

Geophysical Laboratory and Center for High-Pressure Research, Carnegie Institution of Washington, Washington, DC 20015

Anil K. Singh

Materials Science Division, National Aerospace Laboratories, Bangalore 5600 17, India

(Received 2 June 1999)

Using energy-dispersive x-ray diffraction techniques together with the theory describing lattice strains under nonhydrostatic compression, the behavior of a layered sample of gold and rhenium has been studied at pressures of 14–37 GPa. For gold, the uniaxial stress component t is consistent with earlier studies and can be described by $t = 0.06 + 0.015P$ where P is the pressure in GPa. The estimated single-crystal elastic moduli are in reasonable agreement with trends based on extrapolated low-pressure data. The degree of elastic anisotropy increases as α, the parameter which characterizes stress-strain continuity across grain boundaries, is reduced from 1.0 to 0.5. For rhenium, the apparent equation of state has been shown to be strongly influenced by nonhydrostatic compression, as evidenced by its dependence on the angle ψ between the diffracting plane normal and the stress axis. The bulk modulus obtained by inversion of nonhydrostatic compression data can differ by nearly a factor of 2 at angles of 0° and 90°. On the other hand, by a proper choice of ψ, d spacings corresponding to quasihydrostatic compression can be obtained from data obtained under highly nonhydrostatic conditions. The uniaxial stress in rhenium over the pressure range from 14–37 GPa can be described by $t = 2.5 + 0.09P$. The large discrepancy between x-ray elastic moduli and ultrasonic data and theoretical calculations indicates that additional factors such as texturing or orientation dependence of t need to be incorporated to more fully describe the strain distribution in hexagonal-close-packed metals. [S0163-1829(99)02846-5]

I. INTRODUCTION

High-pressure experiments using a diamond anvil cell provide fundamental information on the equation of state of materials over large ranges of compression. However, there is a lack of detailed characterization of the state of the sample within the high-pressure chamber. By using recently developed theories[1–4] describing lattice strains in an opposed anvil device together with new experimental techniques[5] that allow measurement of strain at any orientation relative to the stress axis, it is now possible to place better constraints on such properties of the sample environment as the deviatoric stress, texturing, and the degree of stress-strain continuity across grain boundaries. Such studies also yield information on material properties including shear strength, the elasticity tensor, and the quasihydrostatic compression curve.

The diamond cell is a uniaxial stress device and truly hydrostatic conditions are only obtained when the sample is contained within a fluid pressure medium. At room temperature, a completely hydrostatic environment cannot be sus-

tained above ~13 GPa due to the freezing of all known pressure media. It has long been recognized that the presence of nonhydrostatic stresses can bias equation of state determinations in an opposed anvil device.[6–8] Figure 1 shows equations of state measured under quasihydrostatic and nonhydrostatic conditions for four materials representative of different classes of solids. In all cases, the nonhydrostatic compression curve yields a volume that lies 10–20 % above the quasihydrostatic curve at a given pressure. As a result, equation of state parameters determined under nonhydrostatic conditions may be incorrect. Experimentally determined high-pressure equation of state parameters are used in modeling planetary interiors, determining thermodynamic stability, and assessing the reliability of first principles calculations of material properties. Results from such studies depend on knowledge of accurate hydrostatic equations of state. Highly accurate equations of state of standards such as Au, NaCl, etc., are needed for use as *in situ* pressure markers in x-ray diffraction studies.[16,17]
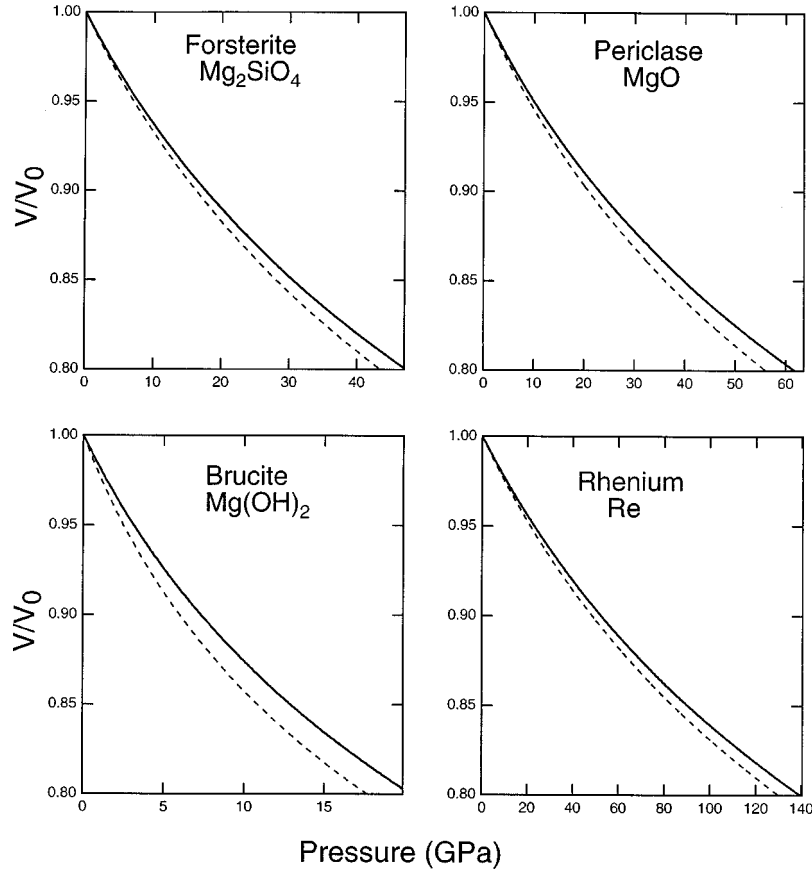
In this study, we examine the behavior of a layered

FIG. 1. Compression curves under nonhydrostatic (solid line) and quasihydrostatic (dashed line) conditions for a representative silicate (forsterite), oxide (periclase), hydroxide (brucite), and metal (rhenium). The hydrostatic curves are obtained from shock data (rhenium) or static compression in a quasihydrostatic medium (helium or neon) (periclase, brucite, forsterite). The nonhydrostatic compression curves were obtained from x-ray measurements on samples with no pressure medium. Pressures are from ruby fluorescence spectra. References: forsterite (Refs. 9 and 10), periclase (Refs. 8 and 11), brucite (Refs. 12 and 13), and rhenium (Refs. 14 and 15).

sample of gold and rhenium under nonhydrostatic loading. Rhenium is a hexagonal-close-packed (hcp) metal with high strength and a large bulk modulus. As a result, rhenium is technically important as a gasket material in ultrahigh-pressure experiments. Gold is a face-centered-cubic (fcc) metal that is characterized by low strength and rigidity. Gold also exhibits a high degree of elastic anisotropy. Because of its low strength, gold is widely used as an *in situ* pressure marker in diamond cell experiments. A preliminary report of this work has been given elsewhere.[18]

II. THEORY

The theory describing lattice strains in a sample nonhydrostatically compressed in the diamond anvil cell has been discussed extensively.[1,2,4,5,19] Here we summarize the main features. The stress tensor in the center of a diamond cell sample can be written as

$$\sigma = \begin{bmatrix} \sigma_1 & 0 & 0 \\ 0 & \sigma_1 & 0 \\ 0 & 0 & \sigma_3 \end{bmatrix} = \begin{bmatrix} \sigma_P & 0 & 0 \\ 0 & \sigma_P & 0 \\ 0 & 0 & \sigma_P \end{bmatrix}$$

$$+ \begin{bmatrix} -t/3 & 0 & 0 \\ 0 & -t/3 & 0 \\ 0 & 0 & 2t/3 \end{bmatrix}, \quad (1)$$

where σ_3 is the principal stress in the axial direction, σ_1 is the principal stress in the radial direction, and σ_P is the mean normal stress or pressure. The second term on the right-hand side of Eq. (1) is the deviatoric stress tensor. The difference between the maximum (σ_3) and minimum (σ_1) stresses is the uniaxial stress component t, which is taken to be positive on compression:

$$t = \sigma_3 - \sigma_1 = 2\tau = Y, \quad (2)$$

where τ is the shear strength and Y the yield strength of the material. The latter two equalities in Eq. (2) hold for a Von Mises yield condition and depend on conditions of plastic flow being reached. In fact, t could be less than the yield strength.

The total lattice strain experienced by a sample under the stress field of Eq. (1) is[4]

$$\epsilon(hkl) = \frac{d_m(hkl) - d_0(hkl)}{d_0(hkl)} = \epsilon_P(hkl) + \epsilon_t(hkl), \quad (3)$$

where $d_m(hkl)$ and $d_0(hkl)$ are the measured d spacings for the lattice plane (hkl) under compression and at ambient pressure, respectively, ϵ_P is the strain component due to hydrostatic pressure, and $\epsilon_t(hkl)$ is the strain produced by the deviatoric stress component.
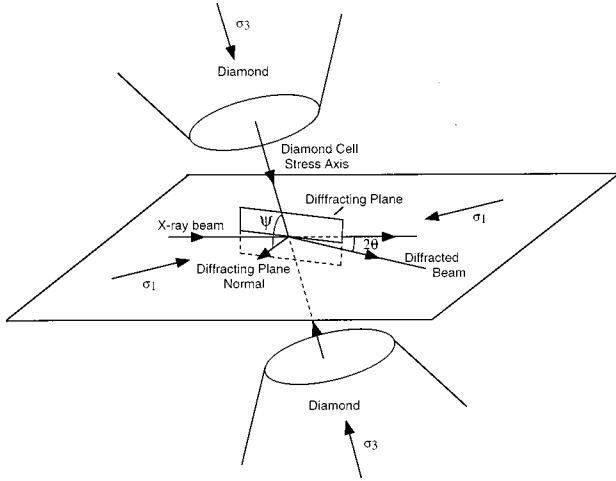
FIG. 2. Experimental geometry for radial diffraction experiments. ψ is the angle between the diamond cell stress axis and the diffraction plane normal. The diffraction angle is 2θ.

The measured d spacing is a function of the angle ψ between the diamond cell stress axis and the diffracting plane normal (Fig. 2):

$$d_m(hkl)=d_p(hkl)[1+(1-3\cos^2\psi)Q(hkl)], \qquad (4)$$

where $d_p(hkl)$ is the interplanar spacing that would result under application of hydrostatic pressure σ_P alone and $Q(hkl)$ is given by

$$Q(hkl)=\frac{t}{3}\left[\frac{\alpha}{2G_R(hkl)}+\frac{1-\alpha}{2G_V}\right]. \qquad (5)$$

$G_R(hkl)$ is the aggregate shear modulus for the crystallites contributing to the diffracted intensity entering the detector under the condition of constant stress across grain boundaries (Reuss limit). G_V is the Voigt (constant strain) bound on the aggregate shear modulus and is not orientation dependent. The parameter α, which varies between 0 and 1, specifies the degree of stress and strain continuity across grains in the sample.

For the cubic system,

$$(2G_R)^{-1}=S_{11}-S_{12}-3S\Gamma(hkl), \qquad (6)$$

where S, a measure of the elastic anisotropy, is given by

$$S=S_{11}-S_{12}-S_{44}/2, \qquad (7)$$

$$\Gamma=\frac{h^2k^2+k^2l^2+h^2l^2}{(h^2+k^2+l^2)^2}, \qquad (8)$$

and

$$(2G_V)^{-1}=\frac{5}{2}\frac{(S_{11}-S_{12})S_{44}}{[3(S_{11}-S_{12})+S_{44}]}, \qquad (9)$$

where the S_{ij} are the isothermal single-crystal elastic compliances.

For the hexagonal system,

$$[G_R(hkl)]^{-1}=(2S_{11}-S_{12}-S_{13})$$
$$+(-5S_{11}+S_{12}+5S_{13}-S_{33}+3S_{44})B(hkl)$$
$$+(3S_{11}-6S_{13}+3S_{33}-3S_{44})B^2(hkl), \quad (10)$$

where

$$B(hkl)=\frac{3a^2l^2}{4c^2(h^2+hk+k^2)+3a^2l^2}, \qquad (11)$$

where a and c are the edge lengths of the hexagonal unit cell.

According to Eq. (4), $d_m(hkl)$ will vary linearly with $1-3\cos^2\psi$. The intercept of the relation gives the d spacing due to the hydrostatic component of the stress. This occurs when $1-3\cos^2\psi$ equals zero or, equivalently, $\psi=54.7°$. At this angle, there is no contribution to the measured d spacing from the deviatoric stress tensor. The slope of $d_m(hkl)$ versus the $1-3\cos^2\psi$ relation yields the product $d_p(hkl)Q(hkl)$.

Equations (4)–(6) also indicate that the plot of $Q(hkl)$ versus $\Gamma(hkl)$ is a straight line for cubic crystals with slope m_1 and intercept m_0 given by

$$m_0=\frac{t}{3}[S_{11}-S_{12}], \qquad (12)$$

$$m_1=-\frac{t}{3}[S_{11}-S_{12}-S_{44}/2], \qquad (13)$$

for the case where $\alpha=1$. More general expressions that hold for any value of α are given elsewhere.[4]

In addition, the linear compressibility χ of a cubic crystal is given by

$$\chi=-\left(\frac{\partial\ln a}{\partial P}\right)_T=\frac{1}{3K}=S_{11}+2S_{12}, \qquad (14)$$

where a is the lattice parameter and K is the isothermal bulk modulus.

These three expressions, together with the relationship between the elastic stiffness and elastic compliance tensors,[20] can be used to write the following expressions for the elastic stiffnesses C_{ij} of a cubic crystal:

$$C_{11}=\frac{1}{3\chi}+\frac{2t}{9m_0}, \qquad (15)$$

$$C_{12}=\frac{1}{3\chi}-\frac{t}{9m_0}, \qquad (16)$$

$$C_{44}=\frac{t}{6(m_0+m_1)}. \qquad (17)$$

In the case of the hexagonal system, Eqs. (4), (5), and (10) indicate that a quadratic relationship between $Q(hkl)$ and $B(hkl)$ is expected. For the case of $\alpha=1$, the three coefficients of the relationship of $Q(hkl)$ and $B(hkl)$ are

$$m_0=\frac{t}{6}(2S_{11}-S_{12}-S_{13}), \qquad (18)$$

$$m_1 = \frac{t}{6}(-5S_{11} + S_{12} + 5S_{13} - S_{33} + 3S_{44}), \quad (19)$$

$$m_2 = \frac{t}{6}(3S_{11} - 6S_{13} + 3S_{33} - 3S_{44}). \quad (20)$$

Again, general expressions for α values other than 1 are given elsewhere.[4] In addition, there are two expressions for the axial compressibility along the a and c axes:

$$\chi_a = S_{11} + S_{12} + S_{13}, \quad (21)$$

$$\chi_c = S_{33} + 2S_{13}. \quad (22)$$

These five equations can be inverted to obtain expressions for the five independent C_{ij}'s of the hexagonal system:

$$C_{11} + C_{12} = \frac{6m + \chi_c t}{\chi_c t(\chi_a - \chi_c) + 3m(\chi_c + 2\chi_a)}, \quad (23)$$

$$C_{11} - C_{12} = \frac{3t}{-t(\chi_a - \chi_c) + 3(3m_0 - m_1 - m_2)}, \quad (24)$$

$$C_{13} = \frac{3m - \chi_c t}{\chi_c t(\chi_a - \chi_c) + 3m(\chi_c + 2\chi_a)}, \quad (25)$$

$$C_{33} = \frac{3m + (3\chi_a - \chi_c)t}{\chi_c t(\chi_a - \chi_c) + 3m(\chi_c + 2\chi_a)}, \quad (26)$$

$$C_{44} = \frac{3t}{t(\chi_a - \chi_c) + 6(3m_0 + 2m_1 + m2)}, \quad (27)$$

where $m = m_0 + m_1 + m_2$.

Thus, by measuring the dependence of interplanar spacing on the angle from the diamond cell stress axis under nonhydrostatic compression, the single-crystal elastic stiffness tensor can be constrained for crystals in the cubic and hexagonal systems. In addition, it is also possible to recover the d spacing and, hence, lattice parameter, for the hydrostatic component of the stress tensor. To solve Eqs. (15)–(17) and (23)–(27) it is necessary know the uniaxial stress t as well as the axial compressibilities. The latter can be determined from the volume compressibility for the cubic system [Eq. (14)] or volume compressibility and the pressure dependence of the c/a ratio in hexagonal crystals:

$$2\chi_a + \chi_c = \frac{1}{K_R}, \quad (28)$$

$$\chi_a - \chi_c = \left(\frac{\partial \ln(c/a)}{\partial P}\right)_T, \quad (29)$$

where K_R is the Reuss bound on the isothermal bulk modulus.

Using Eq. (5), the uniaxial stress component can be determined from

$$t = 6G\langle Q(hkl)\rangle, \quad (30)$$

where $\langle Q(hkl)\rangle$ represents the average value over all observed reflections, and the Reuss bound on the shear modulus is used. The pressure dependence of G_R can be obtained

from extrapolation of ultrasonic or other single-crystal elasticity data. Equation (30) is strictly true only for elastically isotropic materials but t has been shown to depend only weakly on combinations of α and anisotropy.[4]

III. EXPERIMENTAL TECHNIQUE

Experiments were conducted using energy-dispersive synchrotron x-ray diffraction at the bending magnet beam line (13-BM-A) of the GSECARS sector at the Advanced Photon Source. The sample consisted of rhenium powder with a thin gold layer on the upper surface. The gold layer extended to the edges of the gasket hole. The sample was contained within a 50-μm hole in a beryllium gasket and compressed using a diamond anvil cell.

Incident x rays were collimated by a pair of WC slits and focused to 10 μm$\times$10 μm with Kirkpatrick-Baez optics. The size of the incident x-ray beam was measured using a sharp edge. Both the incident and diffracted beams passed through the beryllium gasket, and the sample was positioned such that the x-ray beam passed near the interface of the rhenium and gold layers. The diamond cell was mounted in a rotation stage on a two-circle horizontal diffractometer.[21] The angle ψ between the diffraction plane normal and the diamond cell stress axis was varied from 0° (diffraction plane normal parallel to the diamond cell stress axis) to 90° (diffraction plane normal perpendicular to stress axis) (Fig. 2). The diffracted beam passed through a double-slit system and was detected by a Ge solid-state detector.

At each pressure, energy-dispersive diffraction patterns were recorded at angular intervals of 5°–15°. Diffraction patterns were recorded upon compression at eight pressures between 14.6 and 37.1 GPa and upon decompression at 31.0, 22.3, 21.1, and 15.7 GPa. Hydrostatic pressures were determined from the measured lattice parameter at $\psi = 54.7°$ and the equation of state of gold[22] as discussed below.

Peak positions were obtained by fitting background-subtracted Voigt line shapes to the spectra. For gold, the (111), (200), and (220) diffraction lines were used. The (311) line was partially overlapped at high pressure with lines from the beryllium gasket and was not used in the analysis. For Re, the analysis was based on the following six diffraction lines: (100), (002), (101), (102), (110), and (103).

The method used here differs from conventional energy-dispersive diffraction experiments in which the incident and diffracted x-ray beams pass through the diamond anvils. Due to the limited x-ray access afforded by the backing plates of the diamonds, ψ can be varied only over a small range near $\sim 85°$ in the conventional geometry. Thus, diffraction measurements are confined to near the minimum stress direction. However, by using a beryllium gasket, the diffraction vector can be positioned at any orientation relative to the diamond cell axis.

IV. RESULTS

Figure 3 shows a typical set of diffraction patterns for the Au-Re sample. As the angle increases, the diffraction peaks shift to lower energies as the diffracting plane normal become oriented at higher angles relative to the diamond cell stress axis. At 0°, the diffracting planes are aligned along the
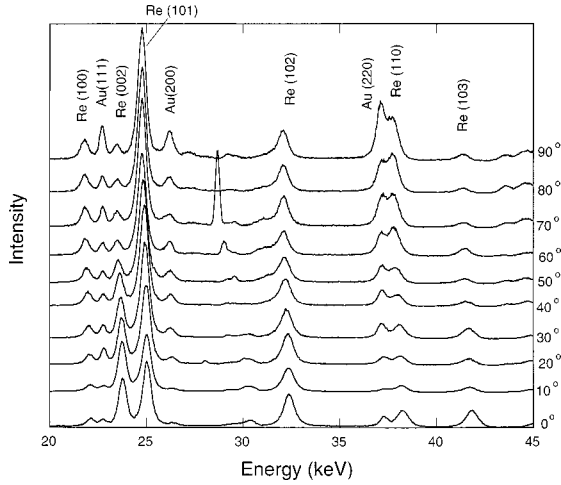
FIG. 3. X-ray diffraction patterns as a function of angle from the stress axis at 37.1 GPa. Diffraction lines from rhenium and gold are labeled. Unlabeled lines are from beryllium. The angle ψ corresponding to each pattern is shown at the right.

maximum stress direction, resulting in the minimum interplanar spacing. The shift in the peak positions is larger for rhenium than for gold because of the larger uniaxial component sustained in the rhenium layer. There are also clear texturing effects illustrated in Fig. 3. The intensity of the rhenium (002) line is strong at low angles and weak at high angles when compared to the neighboring (101) peak. The summed intensity of all (002) peaks is about 32% of the summed intensity of the (101) peaks which is close to the expected value for a random rhenium polycrystal. The preferred orientation of rhenium is typical of that developed during compression of hcp metals, whereby the c axis of the crystallites aligns preferentially along the load direction. Systematic texturing effects are less evident for gold lines. The observed intensity changes may also arise from changes in sample position as the angle is changed. Since the gold layer is very thin, its intensities are especially sensitive to position errors. Changes in peak position will only occur upon sample position changes if there are pressure gradients across the sample. The size of the sample hole was minimized to reduce this effect.

A. Gold

The variation of the d spacing of gold with angle from the diamond cell stress axis is shown in Fig. 4. For all diffraction lines, a linear relationship with $1-3\cos^2\psi$ is observed, in agreement with the predictions of the theory. The (200) peak of gold exhibits a slope that is about twice as great as that of the (111) and (220) peaks which indicates that (200) is an especially sensitive indicator of nonhydrostatic stresses.

The d spacing and lattice parameter corresponding to the purely hydrostatic component of stress, $1-3\cos^2\psi=0$ ($\psi=54.7°$), was determined for each gold diffraction peak (Table I). The standard deviation of the mean lattice parameter determined from the three gold lines was less than 0.1% at this angle. Figure 5 shows the variation of the lattice parameter determined from each diffraction line as a function of $1-3\cos^2\psi$. The (200) line generally yields the smallest lattice parameter at $\psi=0°$ and the largest lattice parameter at
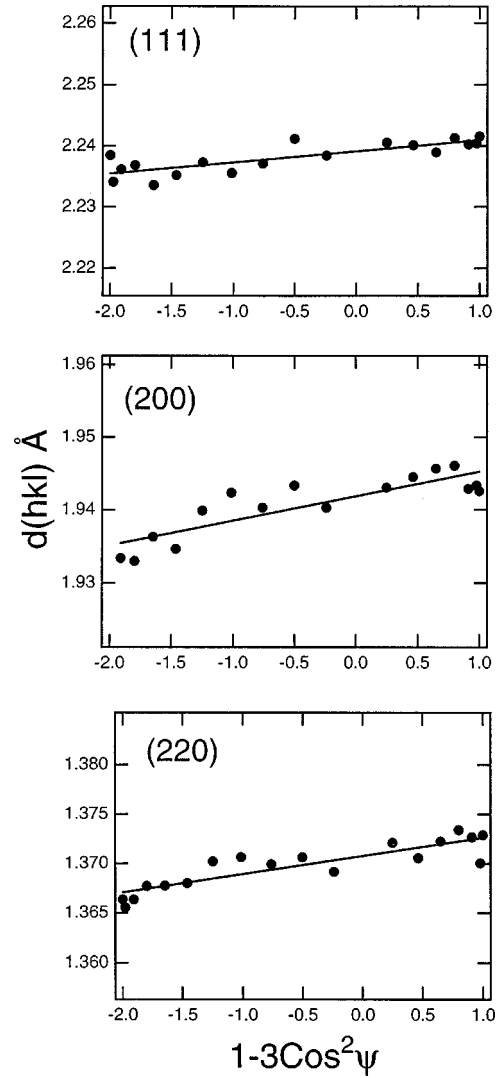

FIG. 4. Dependence of d spacing on $1-3\cos^2\psi$ for diffraction lines of gold at 37.1 GPa. The solid lines are least-squares fits to the data.

$\psi=90°$. The variance in the mean lattice parameter is reduced at 54.7° relative to the 0° and 90° positions. The dependence of $Q(hkl)$ on $3\Gamma(hkl)$ is shown for representative gold data in Fig. 6. In all cases, a linear dependence of $Q(hkl)$ with $3\Gamma(hkl)$ is observed.

Using the equation of state of gold,[22] the pressure was determined from the mean lattice parameter at 54.7° (Table

TABLE I. Lattice parameter and equation of state for gold.

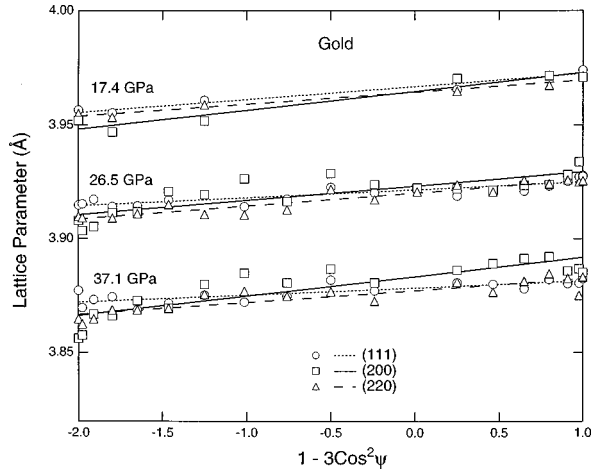| $a(\psi=54.7°)$ (Å)	V/V_0	$P(\psi=54.7°)$ (GPa)	$P(\psi=90°)$ (GPa)	$P(\psi=0°)$ (GPa)
3.9817(11)	0.9304	14.6	12.4	16.8
3.9662(18)	0.9196	17.4	16.1	19.8
3.9459(16)	0.9055	21.5	20.0	23.4
3.9367(27)	0.8992	23.4	21.6	25.7
3.9227(27)	0.8897	26.5	25.3	29.5
3.8984(21)	0.8732	32.3	30.6	36.3
3.8897(26)	0.8674	34.5	31.8	38.7
3.8795(32)	0.8606	37.1	35.4	40.8

FIG. 5. Dependence of lattice parameter on $1-3\cos^2\psi$ for gold at several pressures. The lines are from least-squares fits to the d spacing vs angle data as shown in the previous figure.
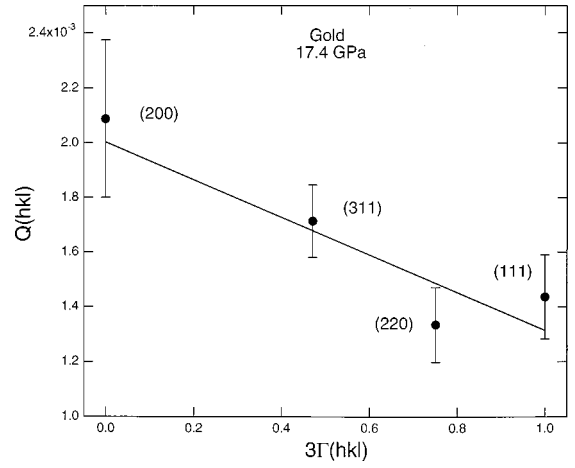

FIG. 6. $Q(hkl)$ as a function of $3\Gamma(hkl)$ for gold at 17.4 GPa. The solid line is a least-squares fit to the data. The estimated errors on $Q(hkl)$ are obtained from the scatter of the $d(hkl)$ vs $1-3\cos^2\psi$ plot.

I). Despite its wide use as an *in situ* pressure marker, the equation of state of gold is not especially well constrained by available data as reported values for $(\partial K_{0T}/\partial P)_T$ vary by $\sim 30\%$.[17] Table II compares aggregate elastic constants of gold and their pressure derivatives from ultrasonic elasticity measurements, static equation of state determinations, and shock compression data. Ultrasonic values for the individual moduli and their pressure derivatives are listed in Table III. The pressure calculated from the various gold equations of state using a third-order Birch-Murnaghan equation range from 46 to 50 GPa at $V/V_0=0.84$, from 88 to 100 GPa at $V/V_0=0.77$, and 167 to 200 GPa at $V/V_0=0.69$. In this study we have used the bulk modulus and pressure derivative from ultrasonic elasticity data of Ref. 22 for the pressure determination. Although the pressure derivatives of the elastic moduli are low in this work relative to other ultrasonic studies, Ref. 22 is in better agreement with static compression and shock data for gold (Table II). It has been observed previously that high-pressure ultrasonic data for simple metals yield pressure derivatives of the bulk modulus that are systematically higher than values derived from shock data.[17] If equations of state based on other ultrasonic data from Table II are used, the pressure may be as much as 10% higher.

Pressures were also calculated from the measured strains at 0° and 90° by assuming that the lattice strain in this di-

rection represents the hydrostatic strain (Table I). The pressures inferred from strain measurements at the minimum and maximum stresses typically differ by about 20%. The pressure under hydrostatic conditions ($\psi=54.7°$) could also be estimated to within better than 0.5 GPa, by simply averaging the apparent pressures calculated along the three principal stress directions:

$$P_{hydro} \approx \frac{(P_0+2P_{90})}{3}. \qquad (31)$$

The uniaxial stress component in gold was calculated using Eq. (30) and the results are in good agreement with earlier diamond cell data[27] (Fig. 7). Between 15 and 37 GPa, the uniaxial stress component of gold ranges between 0.3 and 0.6 GPa. The pressure dependence of the uniaxial stress component of gold from all recent studies can be described by $t=0.06+0.015P$ where P is the pressure in GPa. The value of t is less than the uncertainty in the gold equation of state.

The second-order elastic moduli were determined at each pressure using Eqs. (15)–(17). The results are compared with finite strain extrapolation[29] of ultrasonic elasticity data[22,23] in Fig. 8. The linear compressibility or bulk modulus values were obtained from finite strain[29] extrapolation of ultrasonic

TABLE II. Aggregate elastic moduli and pressure derivatives of gold. The values for Ref. 26 were obtained by fitting the 300-K isotherm to a third-order Birch-Murnaghan equation. K_{0T} is the isothermal, ambient-pressure bulk modulus; G_{VRH} is the Voigt-Reuss-Hill average shear modulus. Numbers in parentheses are one standard deviation uncertainties where available.

Ref.	K_{0T} (GPa)	G_R (GPa)	G_{VRH} (GPa)	G_V (GPa)	$\left(\dfrac{\partial K_{0T}}{\partial P}\right)_T$	$\left(\dfrac{\partial G_R}{\partial P}\right)$	$\left(\dfrac{\partial G_{VRH}}{\partial P}\right)$	$\left(\dfrac{\partial G_V}{\partial P}\right)$
22	167.2	23.8	27.3	30.7	5.21	0.71	0.89	1.06
23	166.3	24.1	27.6	31.1	6.39	0.82	1.04	1.25
24	166.5	24.1	27.6	31.1	6.12	0.84	1.06	1.28
25	166.8	23.7	27.3	30.8	6.26	0.79	1.03	1.27
16	167(11)	-	-	-	5.5(8)	-	-	-
26	171(1)	-	-	-	5.0(1)	-	-	-

TABLE III. Second-order elastic constants and pressure derivatives of gold.

Ref.	C_{11} (GPa)	C_{12} (GPa)	C_{44} (GPa)	$\left(\dfrac{\partial C_{11}}{\partial P}\right)_T$	$\left(\dfrac{\partial C_{12}}{\partial P}\right)_T$	$\left(\dfrac{\partial C_{44}}{\partial P}\right)_T$
22	192.9	163.8	41.5	5.72	4.96	1.52
23	192.2	162.8	42.0	7.01	6.14	1.79
24	192.4	163.0	42.0	6.73	5.89	1.84
25	192.2	163.4	41.8	6.71	5.85	1.83
This study ($\alpha=1$)	-	-	-	6.0	4.3	0.9
This study ($\alpha=0.5$)	-	-	-	5.5	4.5	1.4

data.[22] Thus, a comparison of the results with Ref. 22 (lower dashed curves in Fig. 8) is the most appropriate. Our results for gold are consistent with those of a separate radial diffraction study which examined a layered sample of gold and molybdenum (see Ref. 31).

While C_{11} and C_{12} are in good agreement with ultrasonic data, the values for C_{44} are generally lower than the ultrasonic data. The elastic anisotropy of a cubic crystal can be characterized by the Zener anisotropy ratio A, which is the ratio of shear moduli in the (100) and (110) planes in the [100] direction:

$$A = \frac{2C_{44}}{C_{11}-C_{12}} = \frac{2(S_{11}-S_{12})}{S_{44}} = 1 + \frac{2S}{S_{44}}. \qquad (32)$$

For the case where $\alpha=1$, Eqs. (12)–(14) yield

$$A = \frac{1}{1+m_1/m_0}. \qquad (33)$$

Using the values of m_0 and m_1 from Eqs. (12) and (13), we obtain a mean value of $A=1.8(3)$ at 15–37 GPa. By contrast, the value of A at ambient pressure for gold is 2.9, and the extrapolated values at 14–37 GPa are 3.1–3.4, using

the data of Ref. 22. Thus, the apparent elastic anisotropy determined by x-ray diffraction is much lower than expected on the basis of ultrasonic elasticity. The primary reason for the low anisotropy is the small value of C_{44} determined here. Pressure derivatives obtained from linear fits to the present data combined with ambient pressure data are listed in Table III.

The elastic moduli are sensitive to the choice of α. Figure 9 shows the dependence of the C_{ij}'s on α at 14.6 GPa. While the values of C_{11} and C_{12} are only weakly sensitive to the choice of α, C_{44} increases considerably as α decreases. The inset to Fig. 9 shows the dependence of the anisotropy factor on the choice of α. The anisotropy factor from x-ray data is in agreement with extrapolated ultrasonic values for $\alpha=0.4 \pm 0.1$. Figure 8 also shows the value of C_{44} when $\alpha=0.5$. The anisotropy factor A in this case has a mean value of 3.0 ± 0.7.

If the anisotropy factor is known at high pressure from, for example, sound velocity data, then the x-ray data can be used to constrain the degree of stress or strain continuity across grain boundaries in the sample. A value of $\alpha\sim0.5$ at high pressure was also found in a previous study on NaCl
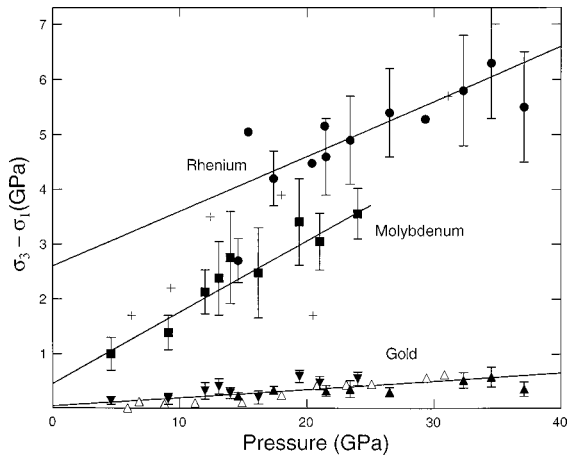

FIG. 7. Uniaxial stress components of metals as a function of pressure. Solid circles are for rhenium with error bars omitted on decompression data. Plus symbols are from measurements of sample pressure gradients for rhenium (Ref. 28). For gold, solid triangles are this study, inverted triangles are from a separate radial diffraction study (Ref. 31), and open triangles are from Ref. 27. Also shown as solid squares are data for molybdenum (Ref. 31). Solid lines are least-squares fits to the data.
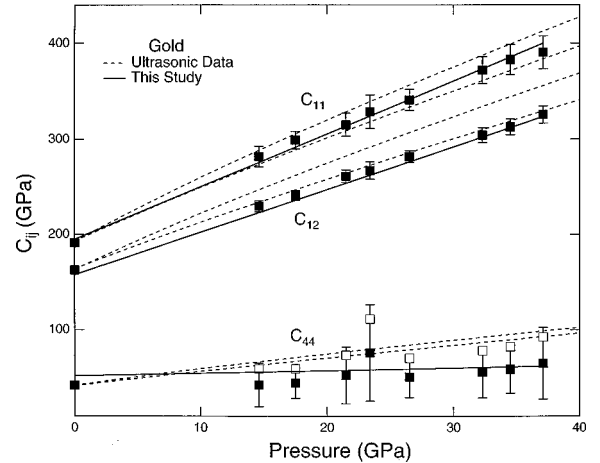

FIG. 8. Second-order elastic moduli of gold as a function of pressure. The symbols show individual data points and solid lines are finite strain fits (Ref. 29) to the present data combined with ambient pressure data (Ref. 22). Uncertainties are one standard deviation. Solid symbols are for $\alpha=1$ and open symbols for C_{44} are for $\alpha=0.5$. The dashed lines show finite strain extrapolations of ultrasonic data (Refs. 22 and 23), where the upper dashed curve corresponds to Ref. 23, and the lower dashed curve is from Ref. 22. The difference between adiabatic and isothermal moduli has been neglected in this comparison.
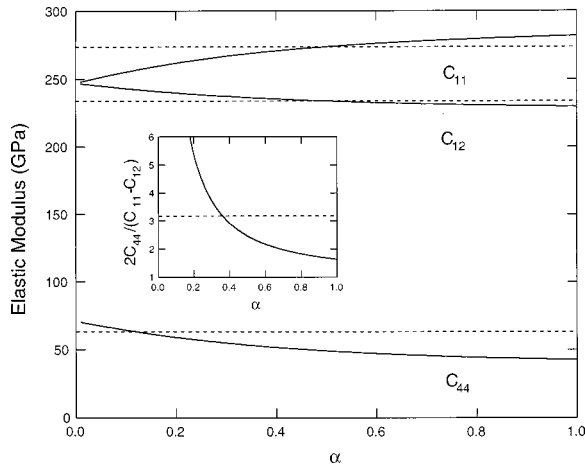
FIG. 9. Elastic moduli of gold as a function of α, the degree of stress-strain continuity across grain boundaries in the sample. The dashed lines show values extrapolated from ultrasonic data at this pressure. The inset shows the dependence of the anisotropy factor on α.

using a modified Drickamer cell.[30] However, in another experiment using a sample of molybdenum and gold and the same diamond cell technique reported here, it was found that reducing α resulted in poorer agreement between ultrasonic

and x-ray elastic constants for molybdenum, a material for which $A < 1$.[31] The value of α is of fundamental importance in high-pressure x-ray experiments since the Reuss condition is assumed to hold when determining the pressure from an *in situ* marker within the sample. With further studies, the present method offers a means to better understand the nature of stress continuity across grain contacts in the high-pressure sample.

B. Rhenium

Figure 10 shows variation of d spacing in rhenium as a function of $1 - 3\cos^2\psi$ at 37.7 GPa. The slopes of the fitting curves vary by a factor of 2.5 for the six different diffraction lines, with (100) yielding the steepest slope and (103) the shallowest slope.

At each angle, a least-squares fit using the six diffraction lines was performed to determine the lattice parameters a and c, and the cell volume. The results at $\psi = 54.7°$ are shown in Fig. 11 and Table IV. The c/a ratio decreases slightly with pressure such that $\partial \ln(c/a)/\partial P = -7.4 \times 10^{-5}$ GPa^{-1}. The value of c/a is largely insensitive to variation of the diffraction vector from the stress axis, and hence is not strongly sensitive to the degree of nonhydrostatic stress. The difference between the c/a at ψ equal to 0° and 90° is less than 0.1%, with a smaller value of c/a gen-
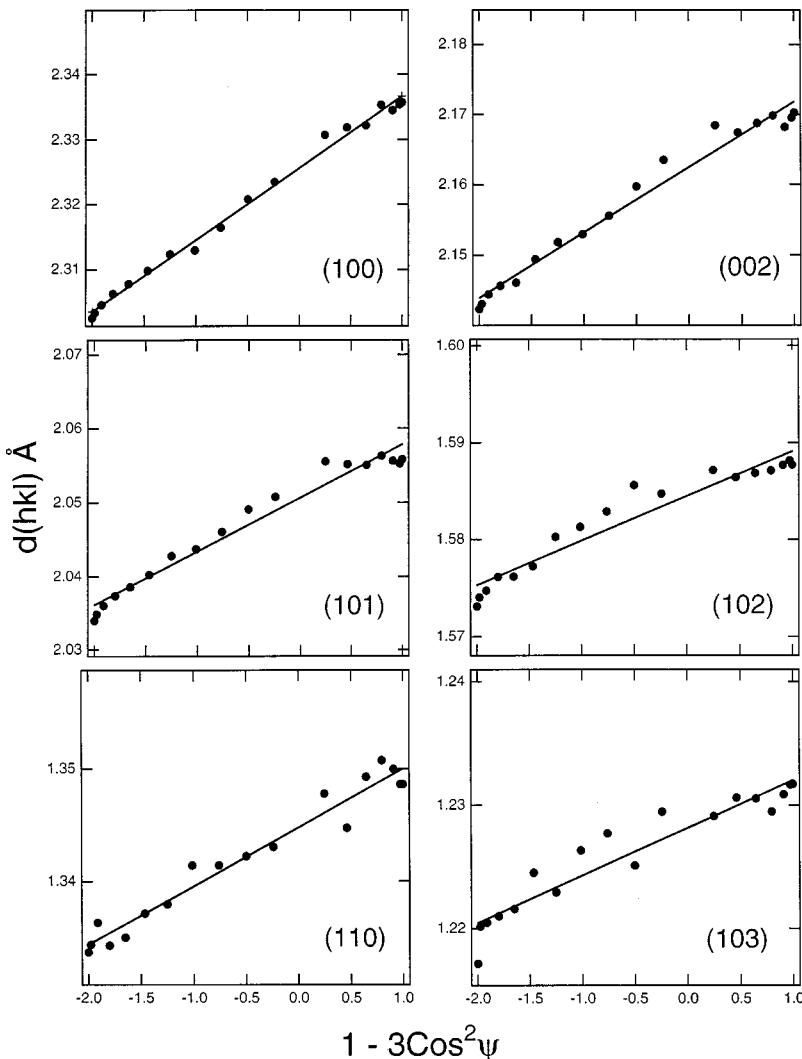

FIG. 10. Variation of d spacing with $1 - 3\cos^2\psi$ for diffraction lines of rhenium at 37.1 GPa. The solid lines are least-squares fits to the data.
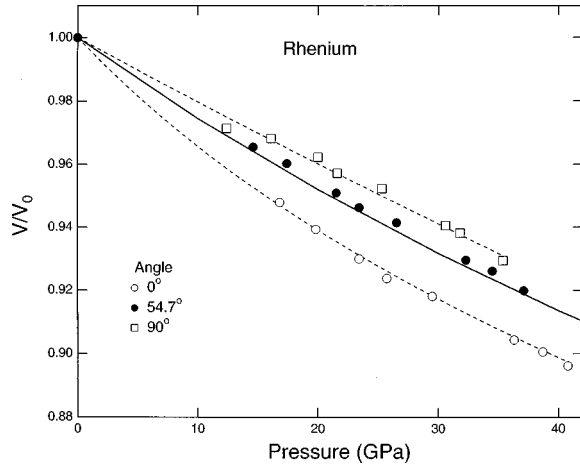
FIG. 11. Equation of state for rhenium from lattice parameters measured at 0°, 54.7°, and 90°. The pressure is determined from the mean lattice parameter of gold. The solid line shows the shock isotherm for rhenium (Ref. 14).

erally measured at 0°. In a previous study of rhenium to 215 GPa, the pressure dependence of c/a was reported to be nearly negligible across this wide pressure range with $\partial \ln(c/a)/\partial P = -9 \times 10^{-7}$ GPa^{-1}.[32]

The initial slope of c/a with pressure can also be calculated from the elastic moduli using Eqs. (21), (22), and (29):

$$\frac{\partial \ln c/a}{\partial P} = \frac{C_{12} + C_{11} - C_{13} - C_{33}}{2C_{13}^2 - C_{33}(C_{11} + C_{12})}. \qquad (34)$$

Using the ambient-pressure elastic moduli of rhenium,[33] this yields $\partial \ln(c/a)/\partial P = -8.0 \times 10^{-6}$ GPa^{-1}, which is of the same sign, but smaller in magnitude than the dependence found here.

The compression curve for rhenium was determined using the pressure determined by the gold marker material at each angle. Equation of state data at 0°, 54.7°, and 90° are shown in Fig. 11 and Table IV. The rhenium equation of state at 54.7° is in good agreement with hydrostatic compression curves constructed from ultrasonic elasticity data[33] and shock compression data[14] in this pressure range. Thus, it is possible to obtain a quasihydrostatic compression curve from these highly nonhydrostatic data by a proper choice of angle between the stress axis and the diffraction vector. However, the data at $\psi = 54.7°$ show a slight systematic deviation from

TABLE IV. Diffraction data for rhenium at $\psi = 54.7°$.

P (GPa)	a (Å)	c (Å)	V (Å^3)	V/V_0	c/a
14.6	2.7287(5)	4.4027(12)	28.3897	0.9655	1.6135
17.4	2.7238(5)	4.3946(13)	28.2358	0.9603	1.6134
21.5	2.7153(2)	4.3790(7)	27.9603	0.9509	1.6127
23.4	2.7112(2)	4.3709(6)	27.8243	0.9463	1.6122
26.5	2.7076(2)	4.3603(4)	27.6832	0.9415	1.6104
32.3	2.6957(4)	4.3432(9)	27.3328	0.9296	1.6112
34.5	2.6920(2)	4.3387(8)	27.2295	0.9261	1.6117
37.1	2.6866(3)	4.3271(8)	27.0479	0.9199	1.6106

TABLE V. Pressure derivatives of elastic moduli of rhenium.

$(\partial M/\partial P)_T$	This study	Ref. 33	Ref. 37	Ref. 14
C_{11}	5.0	8.7	5.5	-
C_{33}	2.3	8.5	6.5	-
C_{12}	2.9	5.5	3.3	-
C_{13}	5.8	3.0	2.5	-
C_{44}	6.1	1.5	1.1	-
C_{66}	1.1	1.6	1.1	-
K_0	4.6	5.4	3.9	4.5

the shock isotherm, with the diamond cell data being less compressible. This could be due to the presence of a residual local deviatoric stress field at the grain-to-grain level.[34,35] Alternatively, the offset may reflect an inconsistency between the shock equation of state of rhenium and the ultrasonic equation of state of gold. Differences in pressure between the gold marker and rhenium sample due to deviation from Reuss conditions may also be responsible for this difference. It should also be noted that changes in the sample position (and hence pressure) as the angle is varied and errors in setting $\psi = 0°$ can also affect the determination of $d_p(hkl)$.[4]

Also shown in Fig. 11 are third-order Birch-Murnaghan equation fits to the data at 0° and 90°. The equations of state at the extreme angles differ greatly and yield equation of state parameters very different from expected values. The ambient-pressure isothermal bulk modulus K_0 of rhenium is 360 GPa,[33] and experimental values for its pressure derivative K_0' are 4.5 (Ref. 14) to 5.4 (Ref. 33) (Table V). The bulk moduli obtained from fits using the third-order Birch-Murnaghan equation at 0° and 90° are 250 GPa and 484 GPa, respectively. Thus, for a strong material such as rhenium, the bulk modulus obtained by inversion of nonhydrostatic compression data can vary be nearly a factor of 2 depending on the relative orientation of the diffraction vector and the diamond cell stress axis. The pressure derivatives obtained from the inversions show an even more extreme variation: from 0.2 at 0° to 10.8 at 90°. This illustrates the strong effect that nonhydrostaticity can have on equation of state parameters. It is also consistent with the results reported in Fig. 1 across a wide range of structure and bonding types.

The hydrostatic equation of state can also be closely reproduced by simple averaging of the pressures and volumes along the principal stress directions. The pressure is computed using Eq. (31) and the volume is averaged according to

$$V_{hydro} \approx \frac{V_0 + 2V_{90}}{3}. \qquad (35)$$

Figure 12 shows the relationship between $Q(hkl)$ and $B(hkl)$ for rhenium. As expected from Eq. (11), the data can be fit well using a quadratic relationship. The uniaxial stresses determined using Eq. (30) are shown in Fig. 7. The t values for rhenium increase linearly with pressure according to $t = 2.5 + 0.09P$ where P is the pressure in GPa. At 30 GPa, the uniaxial stress component in rhenium is 5.2 GPa whereas it is 0.4 GPa in gold at this pressure. Linear extrapolation of
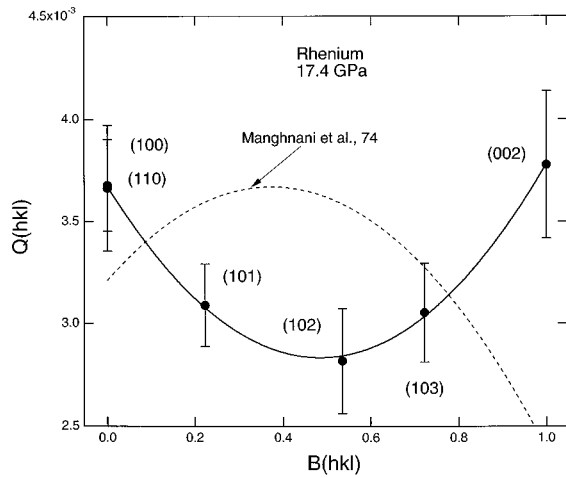
FIG. 12. $Q(hkl)$ as a function of $B(hkl)$ for rhenium at 17.4 GPa. The solid line is a quadratic fit to the data. The dashed line shows the behavior expected based on ultrasonic elastic moduli (Ref. 33) extrapolated linearly to this pressure. The estimated errors on $Q(hkl)$ are obtained from the scatter of the $d(hkl)$ vs 1 $-3\cos^2\psi$ plot.
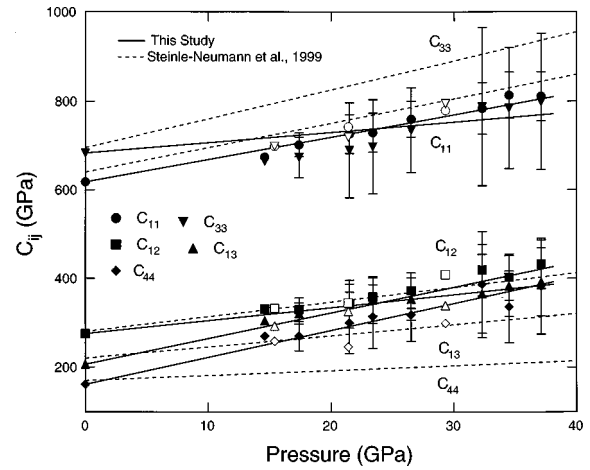
FIG. 13. X-ray elastic moduli of rhenium as a function of pressure. The symbols (solid, loading; open, unloading) show individual data points and the solid lines are fits to the data. Uncertainties for compression data are one standard deviation. Uncertainties for decompression data are not shown for clarity. The dashed lines show linear trends obtained from theoretical calculations of rhenium elastic moduli (Ref. 37). The difference between adiabatic and isothermal moduli has been neglected.

the rhenium results to 100 GPa yields an estimate of $t = 11.5$ GPa at this pressure. This is consistent with the results of recent finite element models of diamond deformation at megabar pressure.[36] In that study, it was found that the yield strength of the gasket material (rhenium) is a key parameter for modeling the observed diamond deformation. The value of the yield strength that best matches the observed data is 12 GPa at a pressure of 100 GPa, which is consistent with the linear trend observed here.

In a previous study, the strength of rhenium was examined by measuring the pressure gradient across the sample and from the pressure offset between the nonhydrostatic and inferred hydrostatic compression curves.[28] The latter method has been shown to overestimate the t value[3] and is not considered further. Figure 7 shows that the present results are generally consistent with data obtained from the pressure gradient across the cell over the common pressure range.

The elastic moduli, estimated using Eqs. (23)–(27), are shown in Fig. 13 and the pressure derivatives obtained from linear fits are shown in Table V. The single-crystal elastic moduli for rhenium from x-ray diffraction are strongly divergent with expectations based on extrapolation of low-pressure ultrasonic data[33] and with theoretical calculations[37] (Table V).

While previous studies of the pressure dependence of rhenium elastic moduli show considerable variability (Table V), the results from the x-ray method cannot be reconciled with earlier data. In particular, the present data yield an unreasonably strong pressure dependence of the moduli C_{13} and C_{44} while the pressure dependence of C_{33} is unexpectedly low. It is of interest to note that those moduli which involve the stress-strain relations in the basal plane (C_{11}, C_{12}, and C_{66}) are consistent with theoretical values. However, those elastic moduli involving the stress-strain response in the meridonal plane (C_{33}, C_{13}, and C_{44}) are highly discrepant with theoretical values. Changing the value of α cannot resolve this discrepancy.[5] Figure 12 compares the measured relation of $Q(hkl)$ and $B(hkl)$ with that predicted from ultrasonic elas-

tic moduli.[33] The expected curvature is the opposite of what is observed. Similar conclusions hold when the theoretical elastic constants[37] are used for comparison.

The large discrepancy between the estimated elastic constants for rhenium from x-ray data with other techniques suggests that additional factors such as preferred orientation (Fig. 2) and the dependence of strength on orientation may need to be accounted for. Further studies are necessary to resolve this discrepancy.

V. SUMMARY

In this study, x-ray diffraction techniques have been developed which allow for measurement of lattice strains as a function angle from the stress axis under nonhydrostatic compression to very high pressures. By using an x-ray transparent gasket with a diamond anvil cell, a more complete picture of the strain distribution and conditions within the high-pressure sample chamber has emerged. The technique can provide otherwise unavailable information on deviatoric strain, yield strength, single-crystal elastic moduli, quasihydrostatic equations of state, texturing, and stress-strain continuity. The lattice strain method has been successfully applied here to a gold/rhenium layered sample to 37 GPa. Future developments are required to improve the precision of elastic modulus and strength determinations and to reconcile discrepancies between the theory and expected values for the elastic moduli of hexagonal-close-packed metals.

ACKNOWLEDGMENTS

---

[1] A. K. Singh, J. Appl. Phys. **73**, 4278 (1993).

[2] A. K. Singh, J. Appl. Phys. **74**, 5920 (1993).

[3] A. K. Singh and C. Balasingh, J. Appl. Phys. **75**, 4956 (1994).

[4] A. K. Singh, C. Balasingh, H. K. Mao, R. J. Hemley, and J. Shu, J. Appl. Phys. **83**, 7567 (1998).

[5] A. K. Singh, H. K. Mao, J. Shu, and R. J. Hemley, Phys. Rev. Lett. **80**, 2157 (1998).

[6] A. K. Singh and G. C. Kennedy, J. Appl. Phys. **45**, 4686 (1974).

[7] G. L. Kinsland and W. A. Bassett, J. Appl. Phys. **48**, 978 (1977).

[8] T. S. Duffy, H. K. Mao, and R. J. Hemley, Phys. Rev. Lett. **74**, 1371 (1995).

[9] G. Will, W. Hoffbauer, E. Hinze, and J. Lauterjung, Physica B&C **139&140**, 193 (1986).

[10] R. T. Downs, C. S. Zha, T. S. Duffy, and L. W. Finger, Am. Mineral. **81**, 51 (1996).

[11] C. S. Zha (unpublished data).

[12] Y. Fei and H. K. Mao, J. Geophys. Res. **98**, 11 875 (1993).

[13] T. S. Duffy, J. Shu, H. K. Mao, and R. J. Hemley, Phys. Chem. Miner. **22**, 277 (1995).

[14] R. G. McQueen, S. P. Marsh, J. W. Taylor, J. N. Fritz, and W. J. Carter, in *High-velocity Impact Phenomena*, edited by R. Kinslow (Academic, San Diego, 1970), p. 294.

[15] J. Hu (unpublished data).

[16] D. L. Heinz and R. Jeanloz, J. Appl. Phys. **55**, 885 (1984).

[17] T. S. Duffy and Y. Wang, in *Ultra-high Pressure Mineralogy*, edited by R. J. Hemley [Rev. Mineral. **37**, 425 (1998)].

[18] T. S. Duffy, G. Shen, D. L. Heinz, Y. Ma, R. J. Hemley, and H. K. Mao, in *High-Pressure Materials Research*, edited by R. M. Wentzcovitch, R. J. Hemley, W. J. Nellis, and P. Y. Yu (MRS Symposia Proceedings No. 499 (Materials Research Society, Warrendale, PA, 1999), p. 145.

[19] T. Uchida, N. Funamori, and T. Yagi, J. Appl. Phys. **80**, 739 (1996).

[20] J. F. Nye, *Physical Properties of Crystals* (Oxford University Press, London, 1975).

[21] M. L. Rivers, T. S. Duffy, Y. Wang, P. J. Eng, S. R. Sutton, and G. Shen, in *Properties of Earth and Planetary Materials*, edited by M. H. Manghnani and T. Yagi (AGU, Washington D.C., 1998), p. 79.

[22] Y. Hiki and A. Granato, Phys. Rev. **144**, 411 (1966).

[23] W. B. Daniels and C. S. Smith, Phys. Rev. **111**, 713 (1958).

[24] B. Golding, S. C. Moss, and B. L. Averbach, Phys. Rev. **158**, 637 (1967).

[25] S. N. Biswas, P. Van't Klooster, and N. J. Trappeniers, Physica B **103**, 235 (1981).

[26] J. C. Jamieson, J. N. Fritz, and M. H. Manghnani, in *High-Pressure Research in Geophysics*, edited by S. Akimoto and M. H. Manghnani (Center for Academic Publications, Tokyo, 1977), p. 27.

[27] Y. Meng, D. J. Weidner, and Y. Fei, Geophys. Res. Lett. **20**, 1147 (1993).

[28] R. Jeanloz, B. K. Godwal, and C. Meade, Nature (London) **349**, 687 (1991).

[29] F. Birch, J. Geophys. Res. **83**, 1257 (1978).

[30] N. Funamori, T. Yagi, and T. Uchida, J. Appl. Phys. **75**, 4327 (1994).

[31] T. S. Duffy, G. Shen, J. Shu, H. K. Mao, and R. J. Hemley, J. Appl. Phys. (to be published).

[32] Y. K. Vohra, Phys. Rev. B **36**, 9790 (1987).

[33] M. H. Manghnani, K. Katahara, and E. S. Fisher, Phys. Rev. B **9**, 1421 (1974).

[34] D. J. Weidner, Y. Wang, and M. T. Vaughan, Geophys. Res. Lett. **21**, 753 (1994).

[35] N. Furnamori, M. Funamori, R. Jeanloz, and N. Hamaya, J. Appl. Phys. **82**, 142 (1997).

[36] S. Merkel, R. J. Hemley, and H. K. Mao, Appl. Phys. Lett. **74**, 656 (1999).

[37] G. Steinle-Neumann, L. Stixrude, and R. E. Cohen, Phys. Rev. B **60**, 791 (1999).